

www.acsami.org Research Article

# Flexible Strain Sensors Based on an Interlayer Synergistic Effect of Nanomaterials for Continuous and Noninvasive Blood Pressure Monitoring

Lin Yuan, Xiaoguang Gao,\* Ranran Kang, Xiaoliang Zhang, Xuejuan Meng, Xiaochun Li,\* and Xiujun Li\*



Cite This: ACS Appl. Mater. Interfaces 2024, 16, 26943-26953



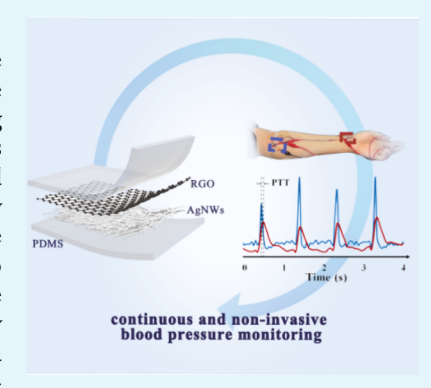
**ACCESS** I

III Metrics & More

Article Recommendations

Supporting Information

ABSTRACT: The continuous, noninvasive monitoring of human blood pressure (BP) through the accurate detection of pulse waves has extremely stringent requirements on the sensitivity and stability of flexible strain sensors. In this study, a new ultrasensitive flexible strain sensor based on the interlayer synergistic effect was fabricated through drop-casting and drying silver nanowires and graphene films on polydimethylsiloxane substrates and was further successfully applied for continuous monitoring of BP. This strain sensor exhibited ultrahigh sensitivity with a maximum gauge factor of 34357.2 (~700% sensitivity enhancement over other major sensors), satisfactory response time (~85 ms), wide strange range (12%), and excellent stability. An interlayer fracture mechanism was proposed to elucidate the working principle of the strain sensor. The real-time BP values can be obtained by analyzing the relationship between the BP and the pulse transit time. To verify our strain sensor for real-time BP monitoring, our strain sensor was compared with a conventional electrocardiogram—photoplethysmograph method and a commercial cuff-



based device and showed similar measurement results to BP values from both methods, with only minor differences of 0.693, 0.073, and 0.566 mmHg in the systolic BP, diastolic BP, and mean arterial pressure, respectively. Furthermore, the reliability of the strain sensors was validated by testing 20 human subjects for more than 50 min. This ultrasensitive strain sensor provides a new pathway for continuous and noninvasive BP monitoring.

KEYWORDS: flexible strain sensor, interlayer synergistic effect, continuous blood pressure monitoring, wearable sensors, graphene

## **■ INTRODUCTION**

Continuous blood pressure (BP) monitoring is of great significance to the health monitoring of critically ill patients in hospitals as well as patients with chronic cardiovascular disease. 1,2 Currently, the most trusted method used clinically is implanted sensors in arteries of the human body to obtain data on the real-time BP of the patient; this methodology is invasive, and inevitably causes significant discomfort and inconvenience to patients.<sup>3,4</sup> The development of a noninvasive, continuous BP monitoring method has thus attracted increasing research attention.<sup>5-9</sup> At present, the most widely studied method in the field of noninvasive, continuous BP monitoring is to accurately measure the pulse transit time (PTT) and obtain the BP values via a relationship linking the PTT and the BP. 10-12 Therefore, the accurate measurement of the PTT is extremely important in the continuous monitoring of the BP. The extraction of the PTT via the photoplethysmograph (PPG) measurement has been successfully utilized in the continuous monitoring of the BP. 11,13,14 The PPG acquisition is usually obtained using optical methods, which consist of additional light sources and photodetectors. However, during PPG, tiny deformations in the device can significantly affect the

optical path, which in turn affects the accuracy of the measurement results. In addition, the integration of the light sources and the photodetectors not only involves a complex fabrication process but also has the characteristics of being high cost. The inherent inflexibility of these optical elements makes it difficult for the sensor to make a good connection with the human body. Therefore, these defects significantly limit the wide application of this technology in the field of continuous BP monitoring.

Recently, flexible strain sensors have greatly facilitated the development of noninvasive and continuous BP monitoring. Compared with piezoelectric and triboelectric sensors, strain sensors have the advantages of a simple preparation method, low cost, easy signal collection, fast response speed, and wide detection range. Piezoelectric and

Received: March 12, 2024
Revised: April 25, 2024
Accepted: April 29, 2024
Published: May 8, 2024





triboelectric sensors have the advantage of operating with a low power consumption. However, these sensors can only detect transient deformations due to the intermittency of piezoelectric and triboelectric effects. Additionally, the fabrication of these sensors often requires complex micropatterning and sophisticated packaging processes. The continuous monitoring of BP using flexible strain sensors involves two steps. The flexible strain sensor is attached to the surface of the skin to obtain the waveform of the pulse wave. Afterward, the BP and PTT values were obtained by extracting the typical characteristic peaks from the pulse waves. Continuous BP monitoring using flexible strain sensors has unique advantages because flexible strain sensors can be perfectly attached to the skin surface, which significantly reduces the discomfort the patient experiences. In addition, flexible strain sensors have the advantages of easy integration, low power consumption, and a simple fabrication process. However, the application of flexible strain sensors for continuous BP monitoring also faces some challenges. For instance, in 2016, Luo et al. achieved continuous monitoring of BP using flexible strain sensors and electrocardiography equipment. 15 The complexity of the system limits its practical application. In 2021, Zhang et al. achieved continuous monitoring of BP by using a flexible strain sensor.<sup>17</sup> During the preparation of the strain sensor, graftmodified multi-walled carbon nanotubes (MWCNTs) and water-based polyurethane were used as the filler and matrix. In addition, the machine learning method was used to analyze the characteristic peaks of the pulse wave and then realized the acquisition of BP. However, limited by the low sensitivity (GF  $\sim$  1582.7) and small strain range (<5%) of the strain sensor, a bandage must be assisted in the process of acquiring the subject's pulse wave waveform, which brings discomfort to the subject. In 2022, Paghi et al. used a sacrificial template method to prepare porous polydimethylsiloxane (PDMS) and directly reduced AgF at room temperature to prepare a flexible piezoresistive sensor. 19 It has a sensitivity of 0.41 kPa<sup>-1</sup>, an operating range of >120 kPa, and a detection limit of 25 Pa. In addition, the piezoresistive sensor can accurately measure the time difference between characteristic peaks when used for pulse wave monitoring, which shows the potential application of the piezoresistive sensor in the field of continuous BP monitoring. The PTT is obtained by identifying the characteristic peaks of the pulse wave, which imposes strict requirements on the sensitivity of the strain sensor. The requirement of high sensitivity is another challenge for strain sensors in continuous BP monitoring. Although existing flexible strain sensors have been successfully used in speech recognition, motion detection, and other fields, they are generally not of sufficient sensitivity for use in continuous BP monitoring.<sup>20–27</sup> Therefore, the development of flexible strain sensors with high sensitivity is of great significance for continuous blood pressure monitoring.

In this study, a new flexible strain sensor with ultrahigh sensitivity was fabricated and successfully applied for continuous, noninvasive BP monitoring. The flexible strain sensor was fabricated through drop-casting and drying silver nanowires (AgNWs) and graphene films on PDMS substrates. The synergistic effect between graphene and the AgNWs endows the sensor with an ultra-high sensitivity. The maximum gauge factor (GF) value of the strain sensor was 34357.2, and the strain range was stretched up to 12%. By observing the surface morphology of the strain sensor under different strain ranges, we proposed an interlayer fracture mechanism to

elucidate the working mechanism of the strain sensor. The strain sensor was successfully employed for the acquisition of the pulse waveform and the determination of the PTT, thereby realizing noninvasive, continuous BP monitoring. The BP values obtained via this noninvasive, continuous BP monitoring system were compared with those obtained from a commercial cuff-based device. The errors obtained for systolic blood pressure (SBP), diastolic blood pressure (DBP), and mean arterial pressure (MAP) were 0.693, 0.073, and 0.566 mmHg, respectively. This study demonstrated that this ultrasensitive flexible strain sensor can be used for noninvasive, continuous BP monitoring with potential applications for hospital diagnostics and daily health care monitoring.

## **■ EXPERIMENTAL SECTION**

Materials. The graphene used in the experiment was prepared by reducing graphene oxide (GO) at a high temperature of 200 °C. The GO powder was purchased from Angstar New Carbon Materials Changzhou Co., Ltd. The sheet diameter and thickness of the GO powder were  $0.1-2 \mu m$  and 1 nm, respectively. The AgNWs dispersion (20 mg/mL) was purchased from Nanjing XFNANO Technology Co., Ltd. The diameter and length of the AgNWs were 90 nm and 20 µm, respectively. The PDMS (Sylgard 184) used in the experiment was obtained from Dow Corning. The ascorbic acid was purchased from Shanghai Aladdin Company. The copper foil used for electrode fabrication was purchased from the Minnesota Mining and Machinery Manufacturing Company. Photographs of the AgNWs and the GO solutions are displayed in Figure S1 (Supporting Information).

Fabrication of the Strain Sensor. The Dow silicone and encapsulants of Sylmar 184 were thoroughly mixed at a mass ratio of 10:1. The mixture was placed in a vacuum-drying oven for 30 min to remove the air bubbles. The PDMS film was deposited via the spincoating method on a pretreated silicon chip and heated at 70 °C for 30 min. Finally, the cured PDMS was tailored to serve as a flexible substrate. The size of the PDMS was 15 mm  $\times$  10 mm  $\times$  0.3 mm. Afterward, the AgNWs and GO layers were sequentially prepared on the PDMS substrate through drop-casting and subsequent drying. The concentrations of AgNWs and GO solutions were both 2 mg/ mL. The volumes of AgNWs and GO solutions were the same as 1 mL. The GO layer was reduced at a temperature of 200 °C for 2 h. In addition, AgNWs and graphene solutions with different concentrations were used for the preparation of the strain sensor. The electrodes of the strain sensor were prepared by coating both ends of the sensing layer with conductive silver paste and attaching a copper foil. Finally, the strain sensor was encapsulated using PDMS of the same size as the substrate.

**Characterization.** The surface morphology of the materials prepared in the study and the strain sensors was characterized by using scanning electron microscopy (SEM, HITACHI, SU8010). The thickness of the graphene and AgNWs layers used in the experiments was measured using atomic force microscopy (AFM, Bruker, Dimension EdgeTM). Raman spectroscopy (Bruker, RAM I1) was conducted to characterize the graphene samples with an excitation wavelength of 532 nm and a power of 50 mW. X-ray diffractometer (XRD, PANalytical, Aeris) and X-ray photoelectron spectroscopy (XPS, Thermo Scientific, ESCALAB Xi+) were used to characterize graphene and AgNWs samples. A motorized stage (Daheng Optics, GCD-502050M) and a SourceMeter (Keithley, 2600B) were used to determine the electromechanical performance of the strain sensor.

## RESULTS AND DISCUSSION

Preparation and Characterization of the Strain **Sensor.** The preparation of the strain sensor includes preparation of the flexible substrate and the sensing layer, fabrication of the electrodes, and encapsulation of the device. Figure 1A shows a schematic diagram of the fabrication

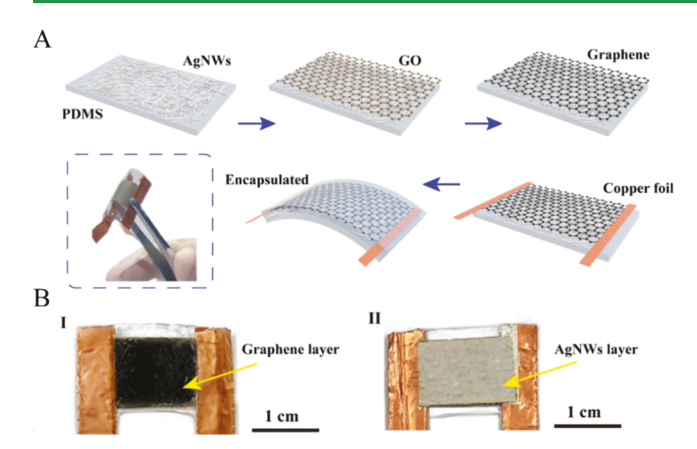


**Figure 1.** Strain sensors based on interlayer synergistic effect. (A) Schematic diagram of the fabrication process of the strain sensor. (B) Photographers of the strain sensor. (I) Front side; (II) Back side.

process of the strain sensor. Both the substrate and packaging materials used in the strain sensor are PDMS. The graphene and AgNWs sensing layers were prepared via drop-coating and subsequent drying. The electrodes of the sensor are composed of conductive silver paste and copper foil. The preparation process is simple and economical. A photograph of the strain sensor held by tweezers is shown in Figure 1A, showing the strain sensor has excellent flexibility, when considering the bending degree of the sensor. Figure 1B(I,II) shows the front and back sides of the strain sensor. It can be seen that the graphene layer and the AgNWs layer of the sensor were fairly uniform.

SEM, AFM, and Raman spectra were used to characterize the morphology of the strain sensor. Figure 2A displays the SEM images of graphene at different magnifications. It can be seen that the graphene surface was fairly smooth. Figure 2B shows SEM images of the AgNWs/graphene conductive film at different magnifications. It can be clearly observed that the AgNWs and graphene were uniformly arranged in layers. The cross-section of the AgNWs/graphene conductive film has been characterized using SEM. It can be clearly observed from Figure S2A,B (Supporting Information) that graphene and AgNWs were arranged in layers. Figure 2C shows the AFM images of graphene, AgNWs, and the AgNWs/graphene conductive film. As can be seen from Figure 2C(I), the graphene prepared via the high-temperature reduction method

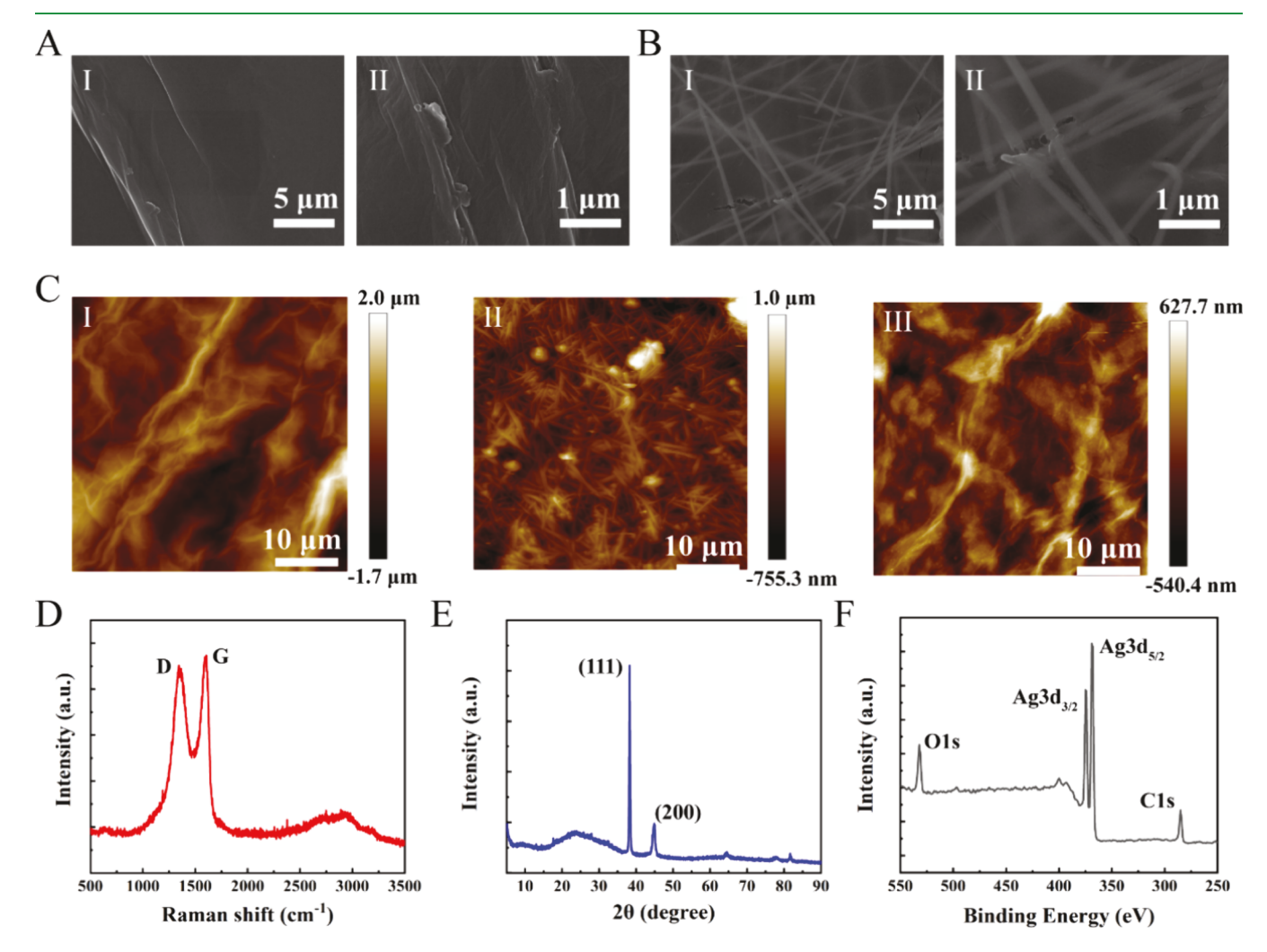


Figure 2. Characterizations of the strain sensor. (A) SEM images of graphene prepared via the high-temperature reduction method at different magnifications. (B) SEM images of the AgNWs/graphene layered structure at different magnifications. (C) AFM images of graphene (I), AgNWs (II), and the AgNWs/graphene layered structure (III). (D) Raman spectrum of graphene prepared via the high-temperature reduction method. (E) XRD patterns of the graphene and AgNWs films. (F) XPS spectrum of the graphene and AgNWs films.

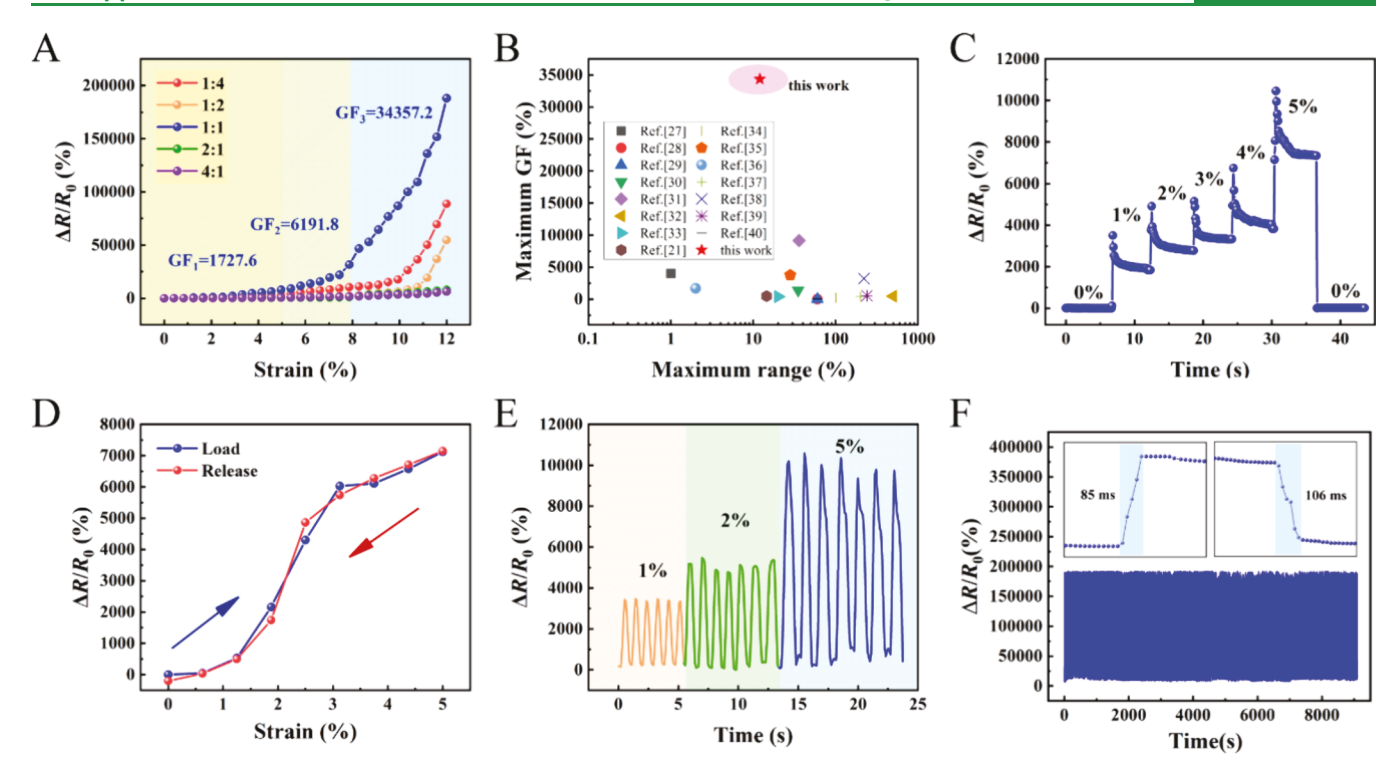


Figure 3. Optimization and characterization of the strain sensor performance. (A) Relative resistance changes versus strain curves of strain sensors with different graphene and AgNWs mass ratios. (B) Comparison of the performance of our strain sensors based on interlayer synergistic effect and other strain sensors reported in the literature. (C) Performance of the strain sensor under 1% strain, 2% strain, 3% strain, 4% strain, and 5% strain, respectively. (D) Relative resistance changes during loading and releasing at 0–5% strain. (E) Dynamic loading-and-releasing cyclic response for 1%, 2%, and 5% strains. (F) Relative resistance changes for 1000 loading-and-releasing cycles of the strain sensor with 12% strain. (Inset shows the response time of the strain sensor).

formed a thin film, while the AgNWs film prepared via dropcoating and subsequent drying formed a dense conductive network, as shown in Figure 2C(II). Figure 2C(III) shows that graphene and AgNWs were arranged in layers. The Raman spectrum of graphene prepared via the high-temperature reduction method is displayed in Figure 2D. The typical G and D bands can be observed at 1590 and 1350 cm<sup>-1</sup>, respectively. The  $I_{\rm D}/I_{\rm G}$  value of  ${\sim}0.95$  also proves the high quality of the prepared graphene samples. For comparison, a chemical reduction method was also used to prepare graphene samples, where the reducing agent used in the experiment was ascorbic acid. The Raman spectrum and SEM were used to characterize the quality of the graphene samples prepared by two methods. Both data from the Raman spectrum and SEM indicate that graphene prepared by the high-temperature method was of higher quality and more uniform, which was important for the performance of the strain sensor. Detailed discussions of graphene preparation methods are included in Supporting Information S3. Figure 2E displays the XRD patterns of the AgNWs and graphene films of the strain sensor. A wide peak located at 26.4° proves that GO was reduced to graphene under high-temperature conditions. The diffraction peaks at 38.2° and 44.2° originate from the AgNWs film, which also proves that the AgNWs were not oxidized under hightemperature conditions. Figure 2F shows the XPS characteristics of the AgNWs and graphene films. It can be observed that it is composed of the elements carbon (C 1s, 284.85 eV), silver (Ag 3d, 368.2 eV, 374.2 eV), and oxygen (O 1s, 532.55 eV). The peaks at 368.2 and 374.2 eV also indicated that the AgNWs were not oxidized under high-temperature conditions.

The AgNWs were not oxidized because the presence of graphene effectively isolates them from contact with air.

Optimization and Determination of the Sensing **Performance.** Studying the performance of the strain sensor is crucial for its application in continuous BP monitoring. The sensitivity of the strain sensor is quantitatively characterized using the GF value.<sup>28</sup> In the following discussion,  $R_0$  is the initial resistance of the strain sensor. R is the real-time resistance of the sensor under strain.  $\triangle R$  represents the resistance to change. Thus,  $\triangle R/R_0$  represents the relative resistance change. Obtaining accurate data on pulse wave waveforms requires a high sensitivity from the strain sensor. To optimize the performance of the sensor, we prepared different strain sensors with different mass ratios of graphene and AgNWs. Figure 3A shows the relative resistance changes as a function of the applied strain for strain sensors with different graphene and AgNWs mass ratios. It can be observed that the signal responses of the strain sensor varied significantly upon changing the mass ratio of the graphene and AgNWs. In terms of sensitivity, the strain sensor had the largest GF value when the mass ratio of graphene to AgNWs was 1:1. The GF value reached 1727.6, 6191.8, and 34357.2 in the strain ranges of 0-5%, 5-8%, and 8-12%, respectively. After confirming that the strain sensor has the maximum GF value when the mass ratio of graphene and AgNWs was 1:1, the effect of concentrations of AgNWs and GO solutions on the performance of the strain sensor was also explored. Figure S4 (Supporting Information) shows the relative resistance changes as a function of the applied strain for strain sensors with different concentrations of AgNWs and GO solutions. During the preparation of these strain sensors, the concentrations of AgNWs and GO were 1.5,

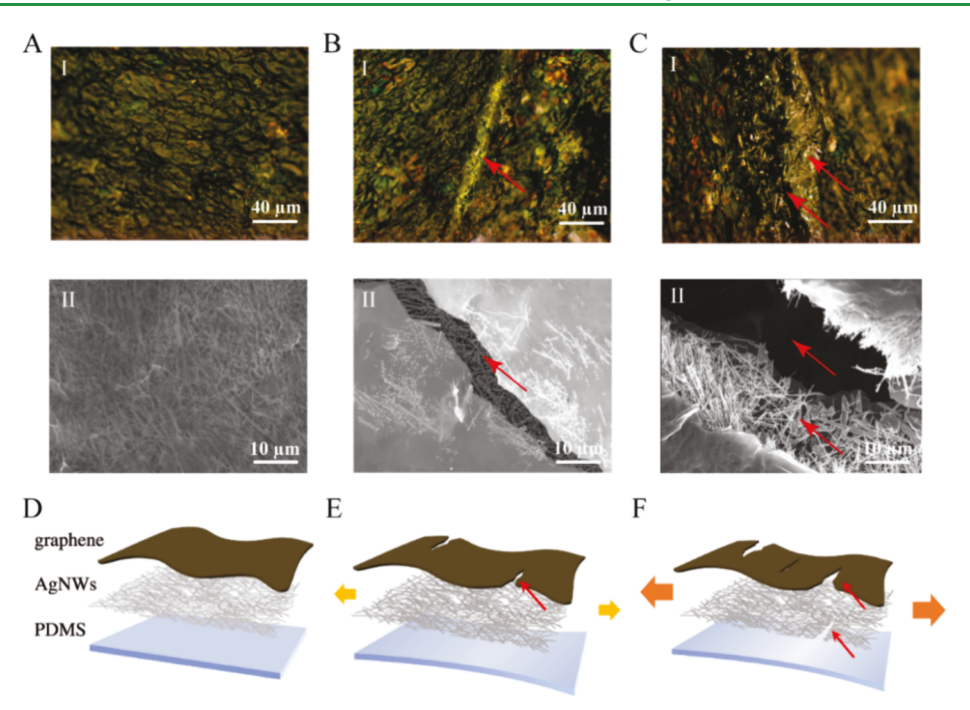


Figure 4. Exploring the sensing mechanism of the strain sensor. (A–C) Optical (I) and SEM (II) images of the surface topography of the strain sensor under different strains (0% strain, 5% strain, and 10% strain). Schematic illustration of the morphology of graphene and silver nanowires under (D) 0% strain. (E) 8% strain and (F) 10% strain.

2.0, 2.5, and 3 mg/mL, respectively. The volumes of AgNWs and GO solutions were both 1 mL. The increase in the concentrations of AgNWs and GO solutions indicates the increase in the mass of conductive material per unit area. When the solution concentration was 1.5 mg/mL, the strain sensor could only withstand a small strain (5.4%). Its maximum GF value was only 3883.2. The reason for the above phenomenon is that there were very few conductive materials per unit area, and a uniform conductive film was not formed. When the concentrations of AgNWs and GO were 2.0, 2.5, and 3 mg/ mL, the strain range and the maximum GF values of these strain sensors were basically the same. It can be concluded that a uniform conductive film was formed at these concentrations. In addition, the maximum GF value of this strain sensor does not change as the mass of the conductive material per unit area increases. In addition, we explored the effect of reduction temperature on the mechanical properties of PDMS and the performance of this strain sensor (Supporting Information S5). It was finally confirmed that the optimal reduction temperature was 200 °C. The GF and stain ranges are the most important parameters for strain sensors. In addition, we compared the performance of this sensor with other strain sensors reported in the literature (Figure 3B). The strain sensors involved in Figure 3B were all prepared by using graphene and AgNWs. It can be clearly seen that our strain sensor exhibited an ultrahigh sensitivity, with maximum GF values 7-fold higher than other majority strain sensors reported in the literature, which provides great potential for the strain sensor to accurately acquire the pulse waveform. Figure 3C shows the signal response of the strain sensor under different strains from 0 to 5% with an incremental step of 1%. It can be observed that for every 1% increase in strain on the sensor, the signal increased by more than 700%. Therefore, the strain sensor is able to distinguish subtle strain changes. The overshoot behavior is clearly observed in Figure 3C at a tensile speed of 4 mm min<sup>-1</sup>. It has been demonstrated that the overshoot behavior

originates from the inherent viscoelastic properties of polymers such as PDMS, TPU, and Ecoflex. In addition, the overshoot behavior will also become more obvious due to the ultrahigh sensitivity of the strain sensor. It also has been proven that the overshoot phenomenon will weaken or even disappear when the strain sensor is in a stable working state. Figure 3D displays the relative resistance changes during loading and releasing at a strain of 0-5%. During the loading and releasing processes, the relative resistance changes were highly similar, which proves that the strain sensor has high stability and good strain memory. It can also be observed that an initial resistance change of less than zero occurs during the release process. The reason for the above phenomenon is that cracks occurred in the graphene and AgNWs films after the strain sensor was stretched and released, which caused its initial resistance to change. Figure 3E shows different relative resistance changes during the multicycle loading-and-releasing process of the strain sensor. The experimental results show that the strain sensor was stable under continuous working conditions. Additionally, the relative resistance changes toward the strain within 12% over 1000 load-and-release cycles were displayed in Figure 3F. Despite the response loss at the beginning of the cycle, more than 90% of the original sensor response remained after 1000 cycles, which confirms the high stability of the strain sensor. The stretching and releasing times for this strain sensor were 85 and 106 ms, respectively. Its high response speed enables the rapid acquisition of pulse wave waveforms. Graphene samples prepared by the high-temperature reduction method and chemical reduction method were used for the fabrication of the strain sensors, respectively. Figure S6 (Supporting Information) shows the relative resistance changes as a function of the applied strain for these strain sensors. In terms of the sensitivity of the strain sensor, it can be observed that graphene prepared by the high-temperature reduction method is superior to graphene prepared by the chemical reduction method. The enhanced sensitivity is mainly

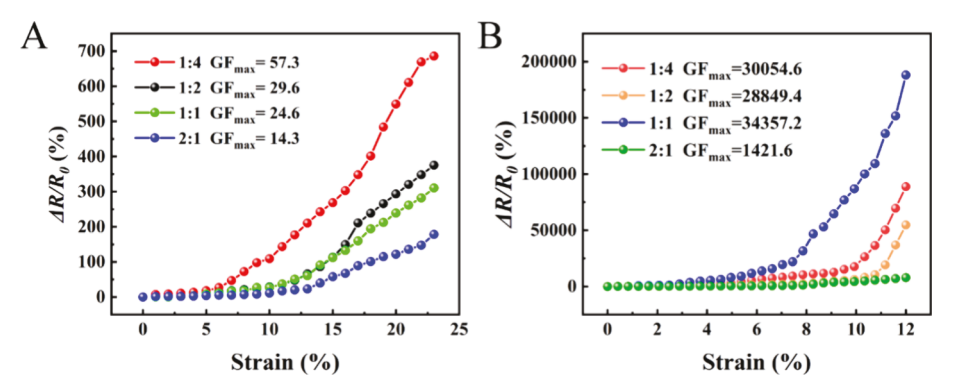


Figure 5. (A) Relative resistance changes strain curves of strain sensors based on AgNWs/graphene mixed particles with different graphene and AgNWs mass ratios. (B) Relative resistance changes strain curves of strain sensors based on an interlayer synergistic effect with different graphene and AgNWs mass ratios.

due to better uniformity from graphene prepared by the hightemperature reduction method, which facilitates the interlayer interaction between graphene and AgNWs. Furthermore, we explored the effects of different sizes of GO and AgNWs on the performance of strain sensors. It has been demonstrated that the performance of strain sensors was not affected by the sizes of GO and AgNWs (Supporting Information S7). Apart from the electromechanical properties of the strain sensor, we also explored the mechanical properties of the strain sensor (Supporting Information S8). Relevant experimental results prove that the strain sensor has excellent recyclability and good strain memory. The reproducibility of the strain sensor preparation method has also been explored in Supporting Information S9. It has been demonstrated that the good reproducibility of the proposed fabrication method (Supporting Information S9). It is also believed that large-scale industrial production processes can reduce the variation in the performance of these strain sensors.

**Sensing Mechanism.** A sensing mechanism based on the interlayer synergistic effect is proposed to explain the working principle of strain sensors. Figure 4A-C shows the surface topography of the strain sensor when it was loaded with different strains. In order to observe the morphology changes of graphene and AgNWs layers, optical microscopy and SEM were used to characterize the strain sensor under different strain ranges. Furthermore, energy-dispersive X-ray spectroscopy (EDS) was also used to characterize the morphology of the strain sensor when it was loaded with different strains. The surface morphology changes of the strain sensor can be observed through imaging carbon (C), oxygen (O), and silver (Ag) elements. The details of the relevant content are shown in Figure S8 (Supporting Information). Based on the above results, we proposed an interlayer fracture mechanism to elucidate the working principle of the strain sensor. Figure 4D-F displays the corresponding schematic diagrams. When no load was applied to the strain sensor, graphene and the AgNWs were layered sequentially. No evident microcracks can be observed on the surface of the film, which proves the good uniformity of the graphene and AgNWs films prepared via drop-casting and subsequent drying.

Figure 4A shows that no microcracks were generated in the graphene and AgNWs layers at a strain range of 0-5%. At this stage, the relative resistance change of the strain sensor is mainly due to the slippage of the graphene sheets. The conductive network composed of AgNWs does not change significantly within this relatively small strain range. As such,

the signal response of the sensor is caused by the contact resistance of the graphene sheets and the AgNWs, which also leads to the lower sensitivity of the sensor in this strain range (GF = 1727.6, as in Figure 3A). Figure 4D shows a schematic diagram of the surface morphology of graphene and AgNWs layers in this strain range. Upon increasing the strain range of the sensor to 5-8% (Figure 4B), several microcracks are generated in the graphene film. No microcracks appeared in the AgNWs film. Figure S10B (Supporting Information) demonstrates that the corresponding elemental mapping images for C and O appeared to be a microcrack, but there was no significant change in the elemental mapping images corresponding to Ag elements. Therefore, when the strain range is 5-8%, the signal response of the strain sensor is caused by the tunneling resistance of the graphene sheets and the contact resistance of the AgNWs. Figure 4E shows a schematic diagram of the surface morphology of graphene and AgNWs layers corresponding to this strain range. The GF value of the strain sensor reached 6191.8 in this strain range. Upon further increasing the strain range to 8-12%, in addition to a clear increase in the number of cracks in the graphene film, microcracks also appeared in the AgNWs film (Figure 4C). As displayed in Figure S10C (Supporting Information), corresponding elemental mapping images for C, O, and Ag elements also show an obvious microcrack. At this stage, the signal response of the strain sensor is due to the tunneling resistance and destruction resistance of the graphene and AgNWs films (Figure 4F); the strain sensor exhibits extremely high sensitivity, and its GF value reached 34357.2 within this strain range (Figure 3A). In addition, the changes in conductive paths of the strain sensor under different strains were illustrated in Figure S11A (Supporting Information). The effect of microcracks in the conductive layers of graphene and AgNWs on the conductive pathways has been discussed in detail. Figure S11B (Supporting Information) shows a model of the basic circuit of the strain sensor. The effect of microcracks in the graphene and AgNWs layers on the change in relative resistance of the strain sensor has been discussed in detail.

To further verify the working principle based on the interlayer synergistic effect of the strain sensor, we prepared different strain sensors based on pure graphene and pure AgNWs. The conductive network of the AgNWs was not easily deformed, which led to a large strain range and a low sensitivity (GF value of 38) of the strain sensor based on the AgNWs (Figure S12A, Supporting Information). The high sensitivity

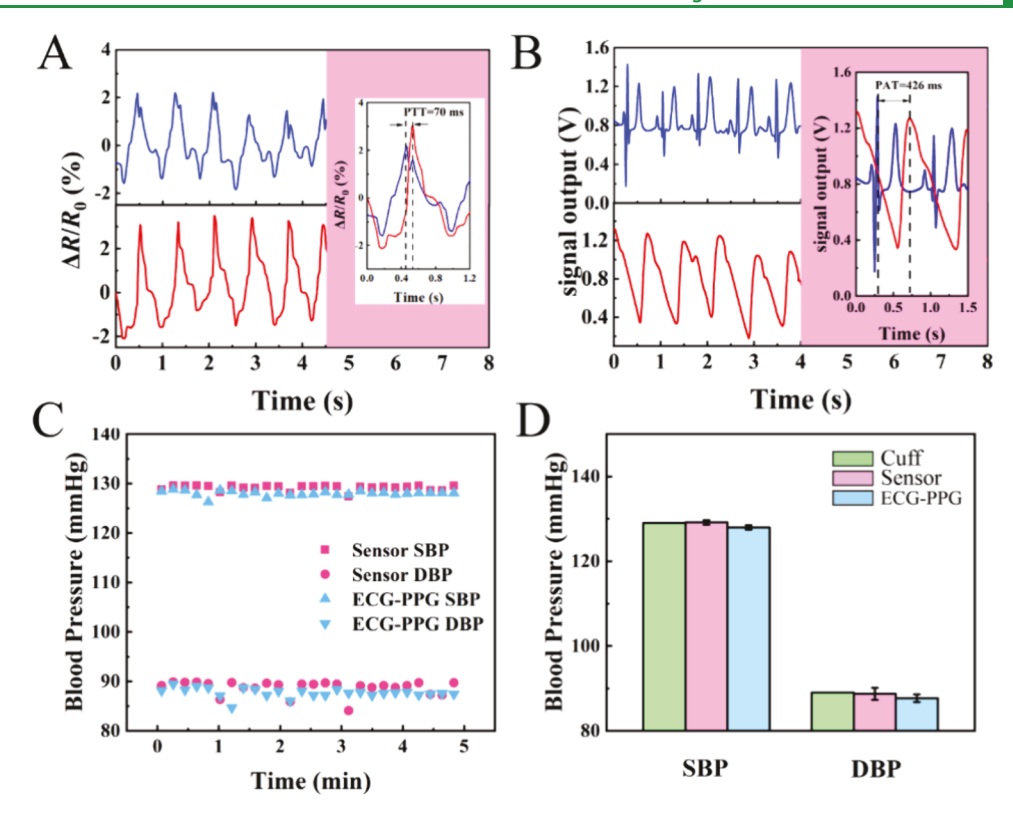


**Figure 6.** (A) Real-time signal responses were obtained when the strain sensors were attached to radial and brachial arteries. Inset shows an enlarged view of the signal for real-time PTT measurement. (B) The real-time signal responses of ECG and PPG. An enlarged view of the signal for real-time PTT measurement. (C) Comparison between the real-time strain sensor monitoring with a method of real-time monitoring SBP and DBP of a human subject achieved by obtaining PTT of ECG-PPG. (D) Comparison between the average SBP and DBP obtained from ECG-PPG and strain sensors for a duration of 5 min and that measured by a commercial cuff-based device.

(GF value of 1355) and the small strain range of the graphenebased strain sensors were due to the fact that graphene is prone to interlayer slippage(Figure S12B, Supporting Information). Furthermore, to demonstrate that it was the layered arrangement of AgNWs and graphene that endowed the strain sensor with ultrahigh sensitivity. The strain sensors based on graphene/AgNWs mixed particles were fabricated to compare with the layered strain sensors. The same mass ratio of graphene and AgNWs was used for the preparation of strain sensors based on AgNWs/graphene mixed particles and interlayer synergistic effect, respectively. The maximum GF values of the strain sensors were directly labeled in Figure 5A, B. In Figure 5A, different mass ratios of graphene and AgNWs were mixed together as the sensing layers of the strain sensor. The strain sensors based on AgNWs/graphene mixed particles with a 1:4 mixing mass ratio of graphene and AgNWs were observed to exhibit the highest GF. However, its maximum GF value was only 57.3. As a comparison, the maximum GF value of the strain sensor based on the interlayer coupling effect at optimal conditions (ratio 1:1) was 34,357.2 (Figure 5B), indicating the synergistic effect from the layered sensor. Additionally, it can be observed that under the same mass ratio of graphene and AgNWs (1:4, 1:2, 1:1, and 2:1), the GF values of the strain sensors based on the interlayer synergy effect are much greater than that of the strain sensors based on AgNWs/ graphene mixed particles. Figure S13 (Supporting Information) shows the SEM images of the graphene/AgNWs mixed particles. During the mixing and reduction processes, graphene attaches to the surface of the AgNWs to form graphene/ AgNWs hybrid particles. Under applied strain, the weak

interaction between hybrid particles exhibited random cracks. With the increase of strain, the size and number of random cracks increased gradually (Figure S14, Supporting Information). Different from the cofracture phenomenon of the graphene and AgNWs in the mixed structure, when graphene and AgNWs were stacked in layers at optimal conditions (ratio 1:1), the strain sensor exhibited ultra sensitivity. It is believed that the interlayer fracture phenomenon (i.e., the interlayer synergy effect) endowed the sensor with ultrahigh sensitivity.

Continuous, Noninvasive BP Monitoring. Continuous, noninvasive BP monitoring can accurately monitor the function of human blood vessels, which is crucial in the diagnosis and treatment of cardiovascular diseases. The application of high-performance flexible strain sensors has prompted significant developments in continuous, noninvasive BP monitoring technology. For the acquisition of data related to BP, PTT is monitored via the use of strain sensors. The real-time calculation of the BP can then be achieved using a quantitative relationship between the BP and the PTT. An in vitro hemodynamic simulator to collect PWV and BP data was developed by Ma et al.<sup>29</sup> by modeling liquid flow through a PDMS (that exhibits a linear stress—strain relationship) tube. A simple expression linking the BP and the PWV was obtained as follows:

$$BP = A \frac{1}{PTT^2} + B \tag{1}$$

where A and B are undetermined coefficients, and the value varies from individual to individual. This expression was used

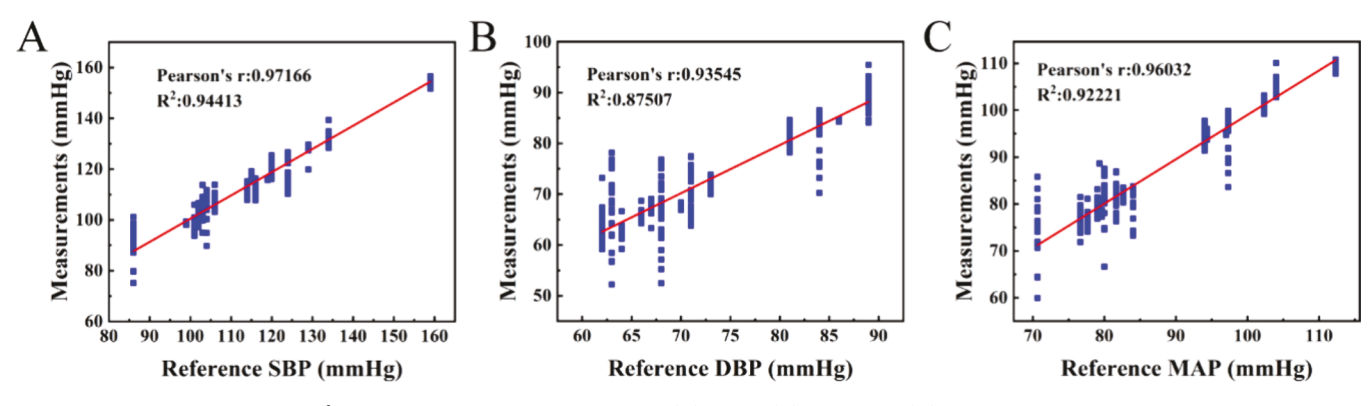


Figure 7. Regression plot with  $R^2 = 0.944$ , 0.875, and 0.922 for SBP (A), DBP (B), and MAP(C), respectively.

in this study to link BP values to PTT for continuous BP monitoring.

The signal obtained from the strain sensor is first processed using a low-pass filter to reduce the presence of noise. The extraction of the characteristic peaks of the pulse wave can then be realized via the acquisition of the pulse waveform; these characteristic peaks are very important for the calculation of the PTT. Finally, the values of the SBP and DBP can be obtained in real time using a quantitative relationship between the BP and the PTT. Figure 6A shows the signal responses when two strain sensors are attached to the radial and brachial arteries, respectively. It can be observed that the characteristic peaks of the brachial and radial pulse waves can be successfully acquired by strain sensors. The inset shows waveforms of radial and brachial arteries during a single cycle. The time difference (70 ms) between the two peaks can be obtained directly from the inset. The accurate measurement of the pulse wave from the data related to the brachial artery is not possible for most strain sensors due to the artery being wrapped inside muscle tissues. The ultrahigh sensitivity of the strain sensor based on the interlayer fracture mechanism enables accurate acquisition of the brachial artery waveform. At the same time, the radial and brachial artery waveforms were monitored for a prolonged period of time using strain sensors, as shown in Figure S15 (Supporting Information). The related results prove that the strain sensor can realize long-term monitoring of radial and brachial artery waveforms. Simultaneous monitoring of radial and brachial artery waveforms using strain transducers is displayed in Video S1 (Support Information).

In addition, the method of obtaining the pulse arrival time (PAT) via electrocardiogram (ECG) and PPG and subsequently obtaining BP data was used to verify the accuracy of the strain sensor-based method. ECG-PPG method is based on the time difference (426 ms) between the R-peak of ECG and a characteristic point of the PPG peak (Figure 6B). Figure 6C shows 5 min of continuous BP monitoring of a human subject using ECG-PGG and strain sensor-based methods. The SBP was maintained at 130 mmHg, where the signal obtained by the ECG-PPG method was slightly lower than that obtained by the sensors, but the maximum error did not exceed 3 mmHg. Meanwhile, the DBP fluctuated at 90 mmHg, and the signal obtained by the ECG-PPGs was also slightly lower than that obtained by the sensors, but the maximum error was within 5 mmHg. It is important to note that all values are stable. Moreover, for SBP and DBP, the ECG-PPG method has the same fluctuation trend as the signal obtained by the sensor.

The strain sensor was further validated by a commercial cuffed device. The mean values of 5 min uncuffed BP monitoring and cuffed BP monitoring were shown in Figure 6D. The SBP and DBP obtained using a commercial, cuffbased device (Yuwell, YE666AR) were 129 and 89 mmHg, respectively. The SBP and DBP obtained via the use of strain sensors based on the interlayer fracture mechanism were  $129.16 \pm 0.54$  and  $88.76 \pm 1.40$  mmHg, respectively. The SBP and DBP values obtained via the ECG-PPG method were  $127.98 \pm 0.50$  and  $87.69 \pm 0.92$  mmHg, respectively. The average DBP and SBP obtained via using the strain sensors show an absolute difference of <2 mmHg compared with the readings provided by the commercial, cuff-based device. It can be seen that the measurement results of the two techniques are highly consistent, validating the accuracy of our strain sensorbased method for continuous BP monitoring.

To further verify the reliability of the strain sensors in BP monitoring, 20 people in the age range from 20 to 60 were studied. The strain sensors were attached to the radial and brachial arteries of each subject to enable the continuous monitoring of the subject's BP. A total of 407 groups of experimental data were obtained. The SBP and DBP of each group were in the ranges of 90-155 and 62-90 mmHg, respectively, which also indicates the included subjects presented clinically defined hypertension and hypotension. Because the pulse wave is a low-frequency signal with a frequency range of less than 5 Hz, the sampling frequency was set to 30 Hz. The sampling time was set to 160 s, and approximately 200 heartbeat cycles were recorded. In addition, MAP was used to verify the reliability of the measurements undertaken using the strain sensors in which MAP is defined as the average of the arterial pressure during a cardiac cycle and can be calculated using the expression:

$$MAP = \frac{SBP + 2 \times DBP}{3}$$
 (2)

It was found that the results of cuffles BP monitoring were in good agreement with those of cuff-based BP monitoring. The error probability distribution was also evaluated. 87% of the estimates were within a 0–5 mmHg error range, 11% were within the error range of 5–10 mmHg, and only 2% of the absolute errors were found to be greater than 10 mmHg (Figure S16, Supporting Information). The results detected by the cuff-based device and the correlation coefficients squared for SBP, DBP, and MAP of the strain sensor-based methods are 0.944, 0.875, and 0.922, respectively, as displayed in Figure 7A–C. In addition, the mean absolute error (MAE) was used to verify the accuracy of the test results. The measured MAE

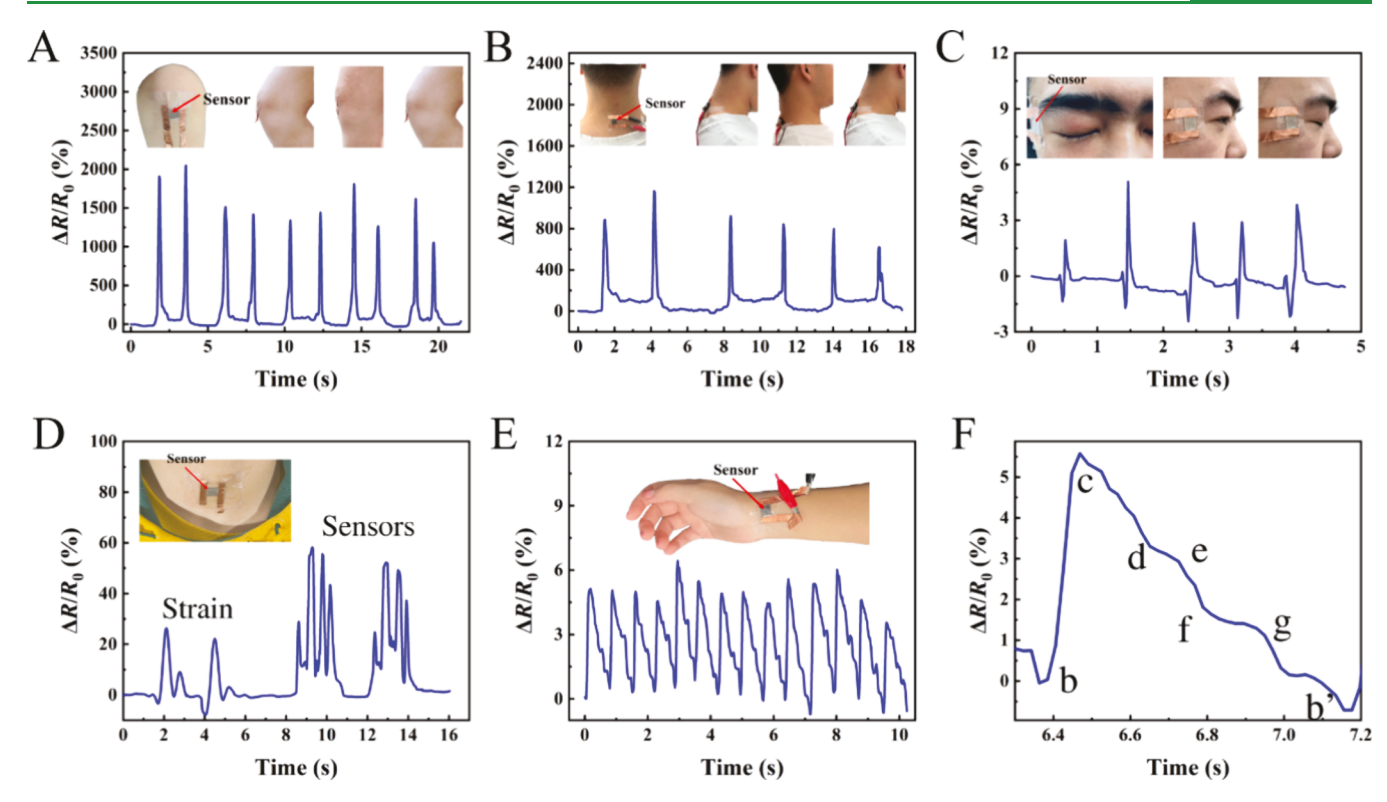


Figure 8. Strain sensors were applied for the detection of subtle and intensive human motions. (A) Relative changes in resistance of walking (the inset shows an image of a leg test in the original state and the bent state). (B) Relative resistance changes in the bending motion of a neck (the inset shows images of the neck test in original state and the bent state). (C) Relative resistance changes of winkling (the inset shows the location of the sensor beside eye). (D) Relative changes in resistance of speaking (the inset shows the location of the sensor on throat). (E) Relative changes in resistance of wrist pulse (the inset shows the location of the sensor on wrist) and (F) the characteristic peaks of the pulse signal.

values for SBP, DBP, and MAP were 2.33, 2.16, and 1.80 mmHg, respectively. Compared with other literature, this study is at the advanced level of previous reports (Table S1, Supporting Information). Table S2 (Supporting Information) shows that the average difference in SBP and DBP of the 20 subjects' parameters between the sensors and Yuwell sphygmomanometer is less than 5%. The above results demonstrate that the use of strain sensors based on the interlayer fracture mechanism can be used to achieve accurate BP monitoring.

Human Physiological Signals Monitoring. After verifying the strain sensor for continuous BP monitoring, the strain sensor was used for real-time monitoring of various physiological signals from different human motions such as knee and neck bending, eye blinking, voice recognition, and pulse wave waveform monitoring. Figure 8A, B shows the signal responses when the strain sensor was attached to the knee and neck, respectively. The strain sensor produced noticeable changes in the signal when the knee and neck were flexed. In addition, benefiting from the ultrasensitivity of the sensor, the strain sensor can accurately capture subtle physiological signals. In Figure 8C, when attached to the skin near the eyes, the strain sensor could detect signal changes caused by eye blinking, which also proves that the strain sensor can be used to monitor changes in human facial expressions. The strain sensor was also successfully used for speech recognition. To explore the possibility of applying the strain sensor in speech recognition, the strain sensor was attached to the human throat. Figure 8D shows the related experimental results. When the human subject said the words "Strain" and "Sensor", the strain sensor showed completely different signal

responses. As displayed in Figure 8E, the strain sensor was used for wrist pulse monitoring. Benefiting from the fast response time which is much lower than a single pulse wavelength time and the ultrahigh sensitivity, the beating of the pulse including systolic and diastolic processes caused a significant change in the resistance of the strain sensor. Figure 8F shows the single pulse waveform monitored by the strain sensor. It can be observed that there are six characteristic peaks in the single-cycle pulse waveform, which is consistent with the existing medical theory. 29,30 All six typical characteristic points such as the systolic peak (b), reflected systolic peak (c), dicrotic notch (d), diastolic peak (e), end-diastolic pressure (f), and dicrotic peak (g) were recorded. The complete acquisition of pulse waveforms is of great significance for the study of the relationship between blood pressure and pulse waveforms. The relevant experimental results prove that the strain sensor cannot only be used for obvious human motion monitoring but also for weak physiological signal monitoring. It can be concluded that the sensors have excellent capability for the healthcare monitoring of various vital signals. As a wearable device, we have explored the impact of hand movement on pulse waveform acquisition. It can be observed that although the strain sensor has been fixed by medical tape during the collection of pulse waveforms, the movement of the hand still causes obvious signal changes (Supporting Information \$17). Therefore, it can be considered that body movement should be avoided when the strain sensor is used for continuous blood pressure monitoring. In addition, with further integration of strain sensors, pulse wave extraction can also be achieved through filtering.

#### CONCLUSIONS

In this study, an ultrasensitive strain sensor based on the interlayer synergistic effect was fabricated by a simple method through drop-coating and drying AgNWs and graphene films on PDMS layers, and this strain sensor was successfully applied for noninvasive continuous blood pressure monitoring. The interaction of the AgNWs and graphene films endowed the strain sensor with ultrahigh sensitivity (GF = 34357.2). In addition, the strain sensor exhibited an excellent response time (~85 ms), an extremely high stability (>300 cycles), and a large strain range ( $\sim$ 12%). We further proposed and verified the interlayer effect mechanism to elucidate the working principle and its high detection sensitivity. In addition, the strain sensors were attached to the brachial and radial arteries to obtain a complete pulse waveform, which enabled the noninvasive, continuous monitoring of the BP. The reliability was confirmed by testing 20 human subjects over 50 min. In this work, the accuracy of the proposed strain sensor-based, continuous BP monitoring technology was validated by comparing the BP values obtained using this method with the data obtained from a commercial cuff-based device and an ECG-PPG method. The proposed strain sensor has numerous advantages, namely, ultrahigh sensitivity simple fabrication process, high reliability, and easy integration; this strain sensor has been demonstrated to have great potential to significantly advance the development of the continuous, noninvasive BP monitoring technology. With the further integration and improvement of the device such as the integration of microfluidic devices and nanosensors, 31-35 the strain sensor based on the synergistic effect can be used in various biomedical settings ranging from hospital diagnostics to daily health care.

### ASSOCIATED CONTENT

## Supporting Information

The Supporting Information is available free of charge at https://pubs.acs.org/doi/10.1021/acsami.4c04134.

Video showing the fixation of the flexible strain sensors and the acquisition process of the pulse waveforms (MP4)

Additional experimental details; materials, and methods; characterizations; additional experimental results (PDF)

#### AUTHOR INFORMATION

## **Corresponding Authors**

Xiaoguang Gao — College of Biomedical Engineering, Taiyuan University of Technology, Taiyuan 030024, China; The Key Laboratory of Weak Light Nonlinear Photonics, Ministry of Education, Nankai University, Tianjin 300071, China; Email: gaoxiaoguang@tyut.edu.cn

Xiaochun Li — College of Biomedical Engineering, Taiyuan University of Technology, Taiyuan 030024, China; orcid.org/0000-0001-6358-9818; Email: lixiaochun@tyut.edu.cn

Xiujun Li — Department of Chemistry and Biochemistry, Forensic Science, & Environmental Science & Engineering, University of Texas at El Paso, El Paso, Texas 79968, United States; ⊕ orcid.org/0000-0002-7954-0717; Email: xli4@ utep.edu

#### **Authors**

Lin Yuan — College of Biomedical Engineering, Taiyuan
University of Technology, Taiyuan 030024, China
Ranran Kang — College of Biomedical Engineering, Taiyuan
University of Technology, Taiyuan 030024, China
Xiaoliang Zhang — College of Biomedical Engineering,
Taiyuan University of Technology, Taiyuan 030024, China
Xuejuan Meng — College of Biomedical Engineering, Taiyuan
University of Technology, Taiyuan 030024, China

Complete contact information is available at: https://pubs.acs.org/10.1021/acsami.4c04134

#### **Notes**

The authors declare no competing financial interest.

#### ACKNOWLEDGMENTS

This work was supported by the Natural Science Foundation of China (21874098, 62005189, 61775157), Key R&D Plan of Shanxi Province (high technologies field, No. 201903D121158), Natural Science Foundation of Shanxi Province (201901D211071), the open foundation of Key Laboratory of Weak Light Nonlinear Photonics from Ministry of Education (OS20-2), the U.S. NIH/NIAID (R41AI162477), the U.S. NSF (IIP2122712, IIP2052347, and CHE2216473), Cancer Prevention and Research Institute of Texas (CPRIT; RP210165), and the DOT (CARTEEH).

# REFERENCES

- (1) MacMahon, S.; Peto, R.; Collins, R.; Godwin, J.; Cutler, J.; Sorlie, P.; Abbott, R.; Neaton, J.; Dyer, A.; Stamler, J. J. T. L. Blood Pressure, Stroke, and Coronary Heart Disease, Prolonged Differences in Blood Pressure: Prospective Observational Studies Corrected for the Regression Dilution Bias. *Lancet* 1990, 335 (8692), 765–774.
- (2) Chobanian, A. V.; Bakris, G. L.; Black, H. R.; Cushman, W. C.; Green, L. A.; Izzo, J. L., Jr; Jones, D. W.; Materson, B. J.; Oparil, S.; Wright, J. T. J. h., Jr Seventh Report of the Joint National Committee on Prevention, Detection, Evaluation, and Treatment of High Blood Pressure. *Hypertension* **2003**, 42 (6), 1206–1252.
- (3) Ding, X.-R.; Zhao, N.; Yang, G.-Z.; Pettigrew, R. I.; Lo, B.; Miao, F.; Li, Y.; Liu, J.; Zhang, Y.-T. Continuous Blood Pressure Measurement from Invasive to Unobtrusive: Celebration of 200th birth anniversary of Carl Ludwig. *IEEE J. Biomed.* **2016**, 20 (6), 1455–1465.
- (4) Cheng, X.; Xue, X.; Ma, Y.; Han, M.; Zhang, W.; Xu, Z.; Zhang, H.; Zhang, H. J. N. E. Implantable and Self-Powered Blood Pressure Monitoring Based on a Piezoelectric Thinfilm: Simulated, in Vitro and in Vivo Studies. *Nano Energy* **2016**, *22*, 453–460.
- (5) Wang, C.; Li, X.; Hu, H.; Zhang, L.; Huang, Z.; Lin, M.; Zhang, Z.; Yin, Z.; Huang, B.; Gong, H.; Bhaskaran, S.; Gu, Y.; Makihata, M.; Guo, Y.; Lei, Y.; Chen, Y.; Wang, C.; Li, Y.; Zhang, T.; Chen, Z.; Pisano, A. P.; Zhang, L.; Zhou, Q.; Xu, S. Monitoring of the Central Blood Pressure Waveform via a Conformal Ultrasonic Device. *Nat. Biomed. Eng.* **2018**, *2* (9), 687–695.
- (6) Lin, H.; Xu, W.; Guan, N.; Ji, D.; Wei, Y.; Yi, W. Noninvasive and Continuous Blood Pressure Monitoring Using Wearable Body Sensor Networks. *IEEE Intell. Syst.* **2015**, *30* (6), 38–48.
- (7) Kaisti, M.; Panula, T.; Leppänen, J.; Punkkinen, R.; Jafari Tadi, M.; Vasankari, T.; Jaakkola, S.; Kiviniemi, T.; Airaksinen, J.; Kostiainen, P. P.; Meriheinä, U.; Koivisto, T.; Pänkäälä, M. Clinical Assessment of a Non-Invasive Wearable MEMS Pressure Sensor Array for Monitoring of Arterial Pulse Waveform, Heart Rate and Detection of Atrial Fibrillation. *npj Digit. Med.* **2019**, 2 (1), 39.
- (8) Sharma, M.; Barbosa, K.; Ho, V.; Griggs, D.; Ghirmai, T.; Krishnan, S. K.; Hsiai, T. K.; Chiao, J.-C.; Cao, H. Cuff-less and Continuous Blood Pressure Monitoring: a Methodological Review. *Technologies* **2017**, *5* (2), 21.

- (9) Jin, Y.; Chen, G.; Lao, K.; Li, S.; Lu, Y.; Gan, Y.; Li, Z.; Hu, J.; Huang, J.; Wen, J.; Deng, H.; Yang, M.; Chen, Z.; Hu, X.; Liang, B.; Luo, J. Identifying Human Body States by Using a Flexible Integrated Sensor. *npj Flex. Electron.* **2020**, *4*, 28.
- (10) Smith, R. P.; Argod, J.; Pépin, J.-L.; Lévy, P. A. Pulse Transit Time: an Appraisal of Potential Clinical Applications. *Thorax* **1999**, 54 (5), 452–457.
- (11) Kim, E. J.; Park, C. G.; Park, J. S.; Suh, S. Y.; Choi, C. U.; Kim, J. W.; Kim, S. H.; Lim, H. E.; Rha, S. W.; Seo, H. S.; Oh, D. J. Relationship Between Blood Pressure Parameters and Pulse Wave Velocity in Normotensive and Hypertensive Subjects: Invasive Study. *J. Hum. Hypertens.* 2007, 21 (2), 141–148.
- (12) Mukkamala, R.; Hahn, J.-O.; Inan, O. T.; Mestha, L. K.; Kim, C.-S.; Toreyin, H.; Kyal, S. Toward Ubiquitous Blood Pressure Monitoring via Pulse Transit Time: Theory and Practice. *IEEE T. Biomed. Eng.* **2015**, *62* (8), 1879–1901.
- (13) Khalid, S. G.; Liu, H.; Zia, T.; Zhang, J.; Chen, F.; Zheng, D. Cuffless Blood Pressure Estimation Using Single Channel Photoplethysmography: A Two-Step Method. *IEEE Access* **2020**, *8*, 58146–58154.
- (14) Li, H.; Ma, Y.; Liang, Z.; Wang, Z.; Cao, Y.; Xu, Y.; Zhou, H.; Lu, B.; Chen, Y.; Han, Z.; Cai, S.; Feng, X. Wearable Skin-like Optoelectronic Systems with Suppression of Motion Artifacts for Cuff-Less Continuous Blood Pressure Monitor. *Natl. Sci. Rev.* **2020**, 7 (5), 849–862.
- (15) Luo, N.; Dai, W.; Li, C.; Zhou, Z.; Lu, L.; Poon, C. C.; Chen, S. C.; Zhang, Y.; Zhao, N. Flexible Piezoresistive Sensor Patch Enabling Ultralow Power Cuffless Blood Pressure Measurement. *Adv. Funct. Mater.* **2016**, 26 (8), 1178–1187.
- (16) Meng, K.; Chen, J.; Li, X.; Wu, Y.; Fan, W.; Zhou, Z.; He, Q.; Wang, X.; Fan, X.; Zhang, Y.; Yang, J.; Wang, Z. L. Flexible Weaving Constructed Self-Powered Pressure Sensor Enabling Continuous Diagnosis of Cardiovascular Disease and Measurement of Cuffless Blood Pressure. *Adv. Funct. Mater.* **2019**, 29 (5), No. 1806388.
- (17) Zhang, Q.; Shen, L.; Liu, P.; Xia, P.; Li, J.; Feng, H.; Liu, C.; Xing, K.; Song, A.; Li, M. J.; Yang, X.; Huang, Y. Highly Sensitive Resistance-Type Flexible Pressure Sensor for Cuffless Blood-Pressure Monitoring by Using Neural Network Techniques. *Compos. Part B-Eng.* 2021, 226, No. 109365.
- (18) Kim, J.; Chou, E. F.; Le, J.; Wong, S.; Chu, M. Khine, Soft Wearable Pressure Sensors for Beat-to-Beat Blood Pressure Monitoring. *Adv. Healthc. Mater.* **2019**, 8 (13), No. 1900109.
- (19) Paghi, A.; Corsi, M.; Corso, S.; Mariani, S.; Barillaro, G. In-Situ Controlled and Conformal Coating of Polydimethylsiloxane Foams with Silver Nanoparticle Networks with Tunable Piezo-Resistive Properties. *Nanoscale Horiz.* **2022**, *7* (4), 425–436.
- (20) Huang, K.; Dong, S.; Yang, J.; Yan, J.; Xue, Y.; You, X.; Hu, J.; Gao, L.; Zhang, X.; Ding, Y. Three-Dimensional Printing of a Tunable Graphene-Based Elastomer for Strain Sensors with Ultrahigh Sensitivity. *Carbon* **2019**, *143*, 63–72.
- (21) Chen, S.; Wei, Y.; Wei, S.; Lin, Y.; Liu, L. Ultrasensitive Cracking-Assisted Strain Sensors Based on Silver Nanowires/Graphene Hybrid Particles. ACS Appl. Mater. Interfaces 2016, 8 (38), 25563–25570.
- (22) Yang, Z.; Wang, D.; Pang, Y.; Li, Y.; Wang, Q.; Zhang, T.; Wang, J.; Liu, X.; Yang, Y.; Jian, J.; Jian, M.; Zhang, Y.; Yang, Y.; Ren, T.-L. Simultaneously Detecting Subtle and Intensive Human Motions Based on a Silver Nanoparticles Bridged Graphene Strain Sensor. ACS Appl. Mater. Interfaces 2018, 10 (4), 3948–3954.
- (23) Tao, L.-Q.; Zhang, K.-N.; Tian, H.; Liu, Y.; Wang, D.-Y.; Chen, Y.-Q.; Yang, Y.; Ren, T.-L. Graphene-Paper Pressure Sensor for Detecting Human Motions. ACS Nano 2017, 11 (9), 8790–8795.
- (24) Pang, Y.; Zhang, K.; Yang, Z.; Jiang, S.; Ju, Z.; Li, Y.; Wang, X.; Wang, D.; Jian, M.; Zhang, Y.; Liang, R.; Tian, H.; Yang, Y.; Ren, T.-L. Epidermis Microstructure Inspired Graphene Pressure Sensor With Random Distributed Spinosum for High Sensitivity and Large Linearity. ACS Nano 2018, 12 (3), 2346–2354.

- (25) Tian, H.; Shu, Y.; Cui, Y.-L.; Mi, W.-T.; Yang, Y.; Xie, D.; Ren, T.-L. J. N. Scalable fabrication of high-performance and flexible graphene strain sensors. *Nanoscale*. **2014**, *6* (2), 699–705.
- (26) Qiu, Z.; Wan, Y.; Zhou, W.; Yang, J.; Yang, J.; Huang, J.; Zhang, J.; Liu, Q.; Huang, S.; Bai, N.; Wu, Z.; Hong, W.; Wang, H.; Guo, C.-F. Ionic Skin with Biomimetic Dielectric Layer Templated from Calathea Zebrine Leaf. *Adv. Funct. Mater.* **2018**, 28 (37), No. 1802343.
- (27) Qiu, D.; Chu, Y.; Zeng, H.; Xu, H.; Dan, G. Stretchable MoS2 Electromechanical Sensors with Ultrahigh Sensitivity and Large Detection Range for Skin-on Monitoring. *ACS Appl. Mater. Interfaces* **2019**, *11* (40), 37035–37042.
- (28) Amjadi, M.; Kyung, K. U.; Park, I.; Sitti, M. Stretchable, Skin-Mountable, and Wearable Strain Sensors and Their Potential Applications: a Review. *Adv. Funct. Mater.* **2016**, 26 (11), 1678–1698.
- (29) Ma, Y.; Choi, J.; Hourlier-Fargette, A.; Xue, Y.; Chung, H. U.; Lee, J. Y.; Wang, X.; Xie, Z.; Kang, D.; Wang, H.; Han, S.; Kang, S.-K.; Kang, Y.; Yu, X.; Slepian, M. J.; Raj, M. S.; Model, J. B.; Feng, X.; Ghaffari, R.; Rogers, J. A. Relation between Blood Pressure and Pulse Wave Velocity for Human Arteries. *Proc. Natl. Acad. Sci. U. S. A.* 2018, 115 (44), 11144–11149.
- (30) Chowienczyk, P. Pulse wave analysis: what do the numbers mean? *Hypertension* **2011**, *57* (6), 1051–1052.
- (31) Tavakoli, H.; Mohammadi, S.; Li, X.; Fu, G.; Li, X. Microfluidic Platforms Integrated with Nano-Sensors for Point-of-Care Bioanalysis. TRAC Trends Anal. Chem. 2022, 157, No. 116806.
- (32) Zhang, J.; Tavakoli, H.; Ma, L.; Li, X.; Han, L.; Li, X. Immunotherapy Discovery on Tumor Organoid-On-a-Chip Platforms That Recapitulate the Tumor Microenvironment. *Adv. Drug Delivery Rev.* 2022, 187, No. 114365.
- (33) Zhou, W.; Dou, M.; Timilsina, S. S.; Xu, F.; Li, X. Recent Innovations in Cost-Effective Polymer and Paper Hybrid Microfluidic Devices. *Lab Chip.* **2021**, *21* (14), 2658–2683.
- (34) Zhou, W.; Fu, G.; Li, X. Detector-Free Photothermal Bar-Chart Microfluidic Chips (PT-Chips) for Visual Quantitative Detection of Biomarkers. *Anal. Chem.* **2021**, *93* (21), *7754–7762*.
- (35) Lv, M.; Zhou, W.; Tavakoli, H.; Bautista, C.; Xia, J.; Wang, Z.; Li, X. Aptamer-Functionalized Metal-Organic Frameworks (MOFs) for Biosensing. *Biosens. Bioelectron.* **2021**, *176*, No. 112947.